Spectrochimica Acta Part A: Molecular and Biomolecular Spectroscopy 251 (2021) 119472

Contents lists available at ScienceDirect

Spectrochimica Acta Part A: Molecular and Biomolecular Spectroscopy

journal homepage: www.elsevier.com/locate/saa

Phyllosilicate-content influence on the spectroscopic properties and antioxidant capacity of Iberian Cretaceous clays

Javier García-Tojal [a,*], Eneko Iriarte [b,*], Susana Palmero [a], María R. Pedrosa [a], Carlos Rad [c], Silvia Sanllorente [a], María Cruz Zuluaga [d], Mónica Cavia-Saiz [e], Dolores Rivero-Perez [e], Pilar Muñiz [e]

[a] Departament of Chemistry, University of Burgos, Plaza Misael Bañuelos s/n, 09001 Burgos, Spain
[b] Human Evolution Laboratory, Department of History, Geography and Communication, University of Burgos, I + D + i Building, Plaza Misael Bañuelos s/n, 09001 Burgos, Spain
[c] Composting Research Group UBUCOMP, E.P.S. La Milanera, University of Burgos, 09001 Burgos, Spain
[d] Departament of Mineralogy and Petrology, University of the Basque Country (UPV/EHU), P.O. Box 644, E-48080 Bilbao, Spain
[e] Departament of Biotechnology and Food Science, University of Burgos, 09001 Burgos, Spain

HIGHLIGHTS

- Kaolinite and muscovite are present in sediments from Utrillas Formation (Spain).
- A new FTIR band-ratio parameter is proposed to infer the illite/kaolinite ratio.
- Fe(III) orthorhombic ions, A and B-Centers and organic radicals are detected.
- Scavenging of DPPH and ABTS radicals depend on the amount of Fe replacing Al.

GRAPHICAL ABSTRACT

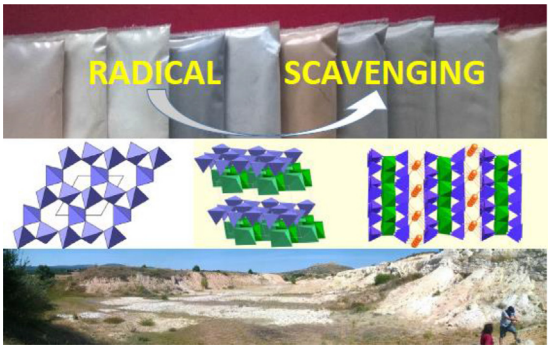

ARTICLE INFO

Article history:
Received 22 October 2020
Received in revised form 8 January 2021
Accepted 11 January 2021
Available online 16 January 2021

Keywords:
Clay minerals
Electron paramagnetic resonance
Infrared spectroscopy
Kaolinite
X-ray diffraction
Antioxidant capacity

ABSTRACT

Kaolinite-rich Cretaceous clay sediment samples from Burgos (Spain) have been analyzed by elemental analysis, X-ray fluorescence, inductively coupled plasma mass spectrometry, X-ray diffraction and different spectroscopic techniques, as Fourier Transform Infrared, ultraviolet–visible and electron paramagnetic resonance. The clay sediment samples mainly contain quartz, muscovite and kaolinite. Different radicals, as A- and B-Centers in kaolinite and organic paramagnetic species, are detected. An illite/kaolinite FTIR band ratio parameter (IKB) is proposed to infer the illite/kaolinite proportion, which can be useful to graphically visualize the iron-substituted Al(III) sites. Studies of the activity as scavengers of DPPH and ABTS radicals show that samples with a larger amount of orthorhombic Fe(III) ions replacing Al(III) ions exhibit a higher antioxidant capacity.

1. Introduction

The properties of sediments containing clay minerals and, therein, their diverse applications strongly depend on the chemical and mineralogical composition as well as the presence of defects in them. Kaolinites, one of the kaolin constituents together with dickite, halloysite and nacrite [1], are among the best studied clay minerals due to interesting features [2]. These and other clays exhibit a wide range of commercial applications in paper industry, paints, ceramics, rubber, plastic, fiberglass, cement, catalysts, molecular sieves, food additives and pharmaceuticals [3–5]. The influence of

* Corresponding authors.
E-mail address: qipgatoj@ubu.es (J. García-Tojal).

https://doi.org/10.1016/j.saa.2021.119472
1386-1425/

the chemical composition, the homogeneity of the particle size and the presence of radicals in the case of kaolinites have been discussed [6,7]. Focusing on their pharmaceutical and dermatological uses, clays have been widely used as excipients, active pharmaceutical ingredients and geomaterials in medicinal thermal muds for pelotherapy [8–18].

Some of the potential therapeutic uses of clay minerals deal with the antiinflamatory properties [19,20], which have been related to the antioxidant activity. Regarding them, it has been found that the inhibition of lipid peroxidation processes, as a result of the lack of stability of hydroxyl HO˙ radical species on the clay surface, is higher in the fibrous palygorskite and sepiolite than in halloysites [21]. On the other hand, the antioxidant activities of muds used for thermal treatments increase during the first six months due to changes in the organic content, to give the so-called mature mud [22]. It is worth noting the risk intrinsic to the presence of toxic inorganic elements, as As, Cd, Cu, Hg, Pb, Se, Te, Tl, in these mixtures [23,24]. Even less toxic ions can cause changes in properties of these minerals. For instance, investigations about foto-oxidation processes on kaolinite surfaces have demonstrated the influence of the iron content on the oxidation of As(III) to As(V) ions [25].

The present work deals with chemical and mineralogical studies performed on ten samples of clay-rich sediments coming from Cretaceous Utrillas Formation (Albian age) at Lara de los Infantes (Burgos, Spain). The Utrillas Formation is a predominantly sandy sequence outcropping in the southern margin of the Basque-Cantabrian Basin (Northern Spain), with abundant clayey intercalations of *fire-clay* type kaolinite-rich clays and kaolinized sand intervals [26–29] (Fig. 1). They have been historically exploted for the manufacture of tiles and porcelain. The clay sediments here analyzed are representative of kaolinite-containing raw clays, in terms of composition and spectroscopic features. The study aims to detect and identify substitution of elements in the clays, and radicals arisen from electron defects. The antioxidant activities are evaluated, and the influence in them of substitution and defects is discussed. A geochemical characterization of these sediments could be useful in order to establish the basis for further geological and palaeontological research and to evaluate potential new uses in pharmaceutical and cosmetic industry.

2. Materials and methods

2.1. Materials

Ten raw clay-rich sediment samples taken from an ancient quarry (42.118140, −3.438923) of middle Cretaceous Utrillas Formation (Albian age) [30] at Lara de los Infantes (Burgos, Spain) were analyzed. The samples were taken every ca. 2 m intervals through a 20 m thick fluvial siliciclastic stratigraphic sequence composed of alternating metric scale channelized fluvial sandstones and flood-plain clayey units (Fig. 1).. The samples were labelled as **L_1** – **L_10**, the abbreviations related to the stratigraphic position of the samples, **LARA_1** is the oldest and **LARA_10** the youngest. The samples were powdered by hand using an agathe mortar (Fig. S.1), except for the oriented aggregates study where they were suspended.

2.2. Methods

2.2.1. Characterization techniques

Elemental analyses (EA) were performed over approximately 1 mg samples in a THERMO FLASH 2000 CHNS analyzer. Semi-quantitative X-ray fluorescence (XRF) analyses were carried out by a Thermo Electron Corporation ARL ADVAT XP Sequential XRF equipment. Pseudo-total content of metal and metalloids in soil samples were determined on 0.2 g of dried and milled sediment samples after microwave assisted digestion (Millestone Ethos One) in 9 mL of concentrated nitric acid and 3 mL concentrated hydrochloric acid (inverted aqua regia mixture) during 30 min at 180 °C. Quantitative element determination was performed in an Inductively Coupled Plasma Optical Emission spectrometer (ICP-OES, Genesis, SPECTRO), operating in radial mode for those elements present in higher amounts, and in an ICP-OES (Arcos, SPECTRO) operating in axial mode, for those in lesser amounts. Internal standard of soil and Calcareous Soil CC690, were used to accomplish the quality control criteria. X-ray diffraction (XRD) data collection was registered on polycrystalline samples in a Bruker D8 Discover Davinci diffractometer equipped with a Cu tube and working at 40 kV, 30 mA, $\lambda Cu_{K\alpha 1}$ = 1,54060 and $\lambda Cu_{K\alpha 2}$ = 1,54439 Å, angular scan (2θ) = 1–70°, stepsize and 1 s time per step.

Oriented aggregate mounts for X-ray powder diffraction were performed in order to carry out a semiquantitative analysis of mineral phases based on XRD intensities. The careful sample preparation was undertaken as follows. Since raw samples showed no effervescence under diluted HCl, decarbonation process was avoided before the separation of the fine clay fraction (<2 μm) to prevent clay minerals alteration. First, an aliquot of each sample was suspended in diluted NH_3 aqueous solution (pH≈8), which was put under ultrasound treatment in order to release the finest particles. Then, the fraction of particles of size < 2 μm was separated and concentrated by centrifugation, and finally, the resulted suspension was decanted over a glass sample holder and dried at room temperature (RT). Four diffractograms were measured for each sample, related to the different chemical treatments: (i) Oriented aggregate without any treatment (AOst). (ii) Oriented aggregate solvated with ethylene glycol for 24 h at RT (AOeg). (iii) Oriented aggregate solvated with dimethyl sulfoxide for 72 h at 80 °C in a stove (AOdm). (iv) Oriented aggregate after thermal

Fig. 1. Outcrops of the sampled clay sediments from an ancient quarry in Lara de los Infantes village (Burgos, Northern Spain).

treatment for 1.5 h at 550 °C in a furnace (AOtt). The simultaneous analysis of the four diffractograms registered for each sample allowed the identification of the different clay minerals present in the < 2 μm fraction. This goal was achieved seeking into the rational series of (00 l) reflections and considering the behavior against the different reactants tested. A semiquantitative approach to the clay-mineral content in the < 2 μm fraction was done following the reflecting powers method, taking into account the intensity ratio of the (00 l) reflections at 10 and 7 Å for illite and kaolinite, respectively [31–33]. Basically, (00 l) reflections in illite show no alteration after any of the treatments performed, while kaolinite expands in AOdm and AOeg, and loses the structure after heated at 550 °C (AOtt) (Fig. 2 a). In the case of the oriented aggregates studies, a PANalythical Xpert PRO diffractometer was used under the following experimental details of data collection: 40 kV, 40 mA, $\lambda Cu_{K\alpha average}$ = 1,541874 Å ($\lambda Cu_{K\alpha1}$ = 1,540598 Å and $\lambda Cu_{K\alpha2}$ = 1,544426 Å), angular scan (2θ) = 1−30°.

Fourier transform infrared spectroscopy (FT-IR) measurements were carried out in the 4000–400 cm^{-1} wavenumber range by a JASCO FT-IR 4200 spectrometer equipped with an attenuated total reflectance (ATR) PRO410-S device. Each spectrum resulted from the accumulation of 128 scans with a 4 cm^{-1} resolution. The intensities of reported IR bands are defined as *vs* = very strong, *s* = strong, *m* = medium and *w* = weak, while *b* means a broad band and *sh* is a shoulder. UV–vis spectra were recorded on powdered solid samples in the λ = 220–850 nm spectral range by a Shimadzu UV-2450 double-bleam spectrophotometer with an integrated sphere ISR-220 attachment. Small amounts of powder samples (<10 mg) were deposited on a transparent colorless quartz disc (diameter 20 mm, thickness 1 mm), pressed by a glass rod, covered by a second quartz disc and mounted over compacted $BaSO_4$, which was likewise used as as blank in the white plate. The spectral resolution was 1 nm. X-band electron paramagnetic resonance (EPR) spectra were registered on polycrystalline samples in a Bruker EMX spectrometer, equipped with a Bruker ER 036TM NMR-teslameter and an Agilent 53150A microwave frequency counter. Variable temperature experiments were controlled by a Bruker ER 4131VT accessory by means of a liquid nitrogen evaporator, a heater and a BVT3000 temperature controller. Simfonia program 1.25 (WINEPR SimFonia, Bruker Analytische Messtecnik GmßH, Karlsruhe, Germany) was used to perform the simulated spectra and graphics were carried out with Kaleidagraph 4.1 Synergy Software: Reading, Pensilvania, USA). Experimental details are given in figure captions.

2.2.2. Total antioxidant capacity

QUENCHER (Q-) versions Q-ABTS, Q-DPPH, and Q-LPSC assays were selected to evaluate the total antioxidant capacity in direct contact with the solid sediment. Quencher procedures are direct approaches withouth extraction. The direct measurements were carried out following the procedure described by Del Pino-García et al. [34]. Three aliquots taken from each sediment sample were used; the results arose from the average of three different spectroscopic measurements performed on each of the aliquots.

2.2.2.1. Q-ABTS, Quencher-2,2′-azinobis(3-ethylbenzothiazoline-6-sulfonic acid), and Q-DPPH (Quencher-2,2-diphenyl-1-picrylhydrazyl) assays. A sample of 250 mg was weighted and mixed with ABTS or DPPH solutions, which were prepared in Milli-Q water or pure methanol, respectively, following a method previously reported [34]. After incubation for 30 min in the dark in an orbital shaker, the supernatant was separated and the absorbances were measured at 734 and 517 nm for ABTS and DPPH, respectively. A linear calibration curve was obtained with different amounts of Trolox ((6-hydroxy-2,5,7,8-tetramethyl-chroman-2-carboxylic acid)) as standard.

2.2.2.2. Q-LPSC assay. This assay was used to evaluate the inhibition of lipid peroxidation. The experiments were carried out in rat liver microsomal preparations [35]. Lipid peroxidation was induced using AAPH, 2,2′-azobis-(2-amidinopropane) dihydrochloride, as oxidant. 500 mg/2 mL of the sediment samples were incubated with 50 μL of microsomal solution and 50 mL of 100 mM APPH solution to 37 °C for 90 min. Afterwards, TCA (trichloroacetic acid, 2.8% w/v) and 500 μL of TBA (2-thiobarbituric acid, 1% w/v) were added and incubated to 100 °C for 15 min. TBA reactive substances were extracted with the same volume of butanol. Then, the absorbance at 532 nm was measured and the results were expressed as oxidation inhibition % with respect to the control withouth sediment sample.

3. Results and discussion

3.1. Chemical characterization

The properties of a clay and its possible biological activity depends, at least in part, on the chemical composition, whose knowledge provides complementary information to elucidate the speciation, i.e. the presence of different compounds as mineral or not mineral phases, the possible element replacement or substitutions and even the underlying reasons for the formation of radical centers in some of the mineral phases contained in the sediments.

The quantitative EA results showed low amounts of C, H, N and S in the studied samples, see Table 1. Hydrogen content was related, at least in part, to the presence of organic matter, water and minerals containing hydroxyde OH^- groups. By the other

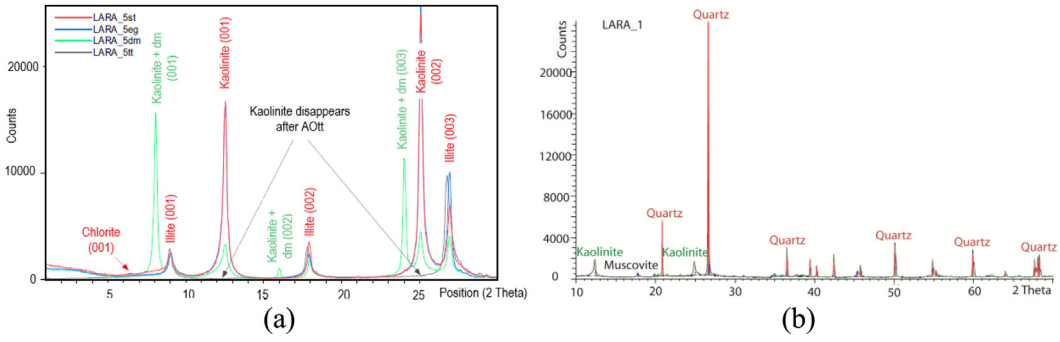

Fig. 2. Representative X-ray diffractograms of a clay fraction sample (a) and a bulk sediment (b). (a) Oriented aggregate diffractograms of **L_5** during the different stages of the chemical treatment: (red) Oriented aggregate without any treatment (AOst). (blue) Oriented aggregate solvated with ethylene glycol (AOeg). (green) Oriented aggregate solvated with dimethyl sulfoxide (AOdm). (grey) Oriented aggregate after thermal treatment (AOtt). (b) Bulk sediment diffractogram of **L_1**.

Table 1
Colors (*Munsell*® color scale), LOI and EA of the different samples analyzed.

Sample	Color	% LOI	%N	%C	%H	%S
L_1	5YR 7/5 *Grayish orange pink*	3.8737	0.00	0.01	0.44	0.00
L_2	5YR 8/4 *Grayish yellow*	4.2107	0.00	0.01	0.45	0.00
L_3	5YR 7/2 *Yellowish gray*	1.4382	0.00	0.00	0.12	0.00
L_4	N4 *Med. dark grey*	6.4665	0.00	1.79	0.51	0.12
L_5	N7 *Light grey*	1.6067	0.00	0.00	0.14	0.00
L_6	5YR 5/6 *Light brown*	4.7889	0.00	0.12	0.61	0.00
L_7	5YR 7/2 *Yellowish gray*	5.4061	0.00	0.71	0.58	0.00
L_8	5YR 6/1 *Light brownish grey*	3.8645	0.00	0.58	0.49	0.00
L_9	N7 *Light grey*	4.0129	0.00	0.27	0.47	0.00
L_10	5YR 7/6 *Moderate yellow*	0.9829	0.00	0.00	0.05	0.00

way, the darkest samples exhibited a greater C-content, mainly **L_4** but also **L_6** – **L_9**. **L_4**, was also the unique one where appreciable amounts of S are present. The loss on ignition (LOI) percentage after 4 h in furnace at 550 °C (LOI) also gave the largest value for **L_4** (Table 1).

Semiquantitative X-ray fluorescence analyses on the solid samples (XRF, Tables 2 and S.1) and quantitative ICP-MS measurements performed on the dissolved fraction of the sediments (Table S2) showed that **L_3**, **L_5** and **L_10** were the samples with the greatest Si content and the poorest in metal elements. On the other hand, **L_6** exhibited the largest amount of Fe and one of the biggest Al content. As a whole, **L_6** - **L_9** and **L_4** exhibited the greatest amounts of U and Th. The thorium amount presented the same trends as the K_2O content (Tables S.2 (c,d)).

3.2. X-ray diffraction

The mineralogical analysis by X-ray powder diffraction (XRD) techniques allowed to identify major crystalline phases present in the samples and, therein, to rationalize some of their bulk properties. Semi-quantitative estimations arising from XRD measurements on bulk samples clearly showed that they maninly contained quartz (38% to 97%) and phyllosilicate minerals (3% to 62%) (Table 3 and Fig. 2). The greatest phyllosilicate content corresponded, ranked in ascending order, to **L_2** (51%), **L_7** (57%) and **L_6** (62%). On the opposite, **L_5** (80%), **L_3** (89%) and **L_10** (97%) are mainly quartz. The quartz content seemed to be related to a higher silt/sand content of the sediment sample.

In order to characterize phyllosilicates present in the samples, analyses of the < 2 μm fraction of the oriented aggregates were carried out. The results are summarized in Table 3 and evidenced the presence of illite (I) and kaolinite (Kaol) clay minerals, as the most abundant phases. Scarce and non-quantifiable amounts of chlorite were detected. In the same way, the comparison of AOst and AOeg diffractograms suggested the presence of interestratified illite–smectite. Other minerals, as goethite and lepidocrocite, FeO(OH), and jarosite, $KFe_3(OH)_6(SO_4)_2$, were identified in some of the samples (Table 3).

3.3. Spectroscopic characterization

3.3.1. FT-IR

The infrared spectroscopy (IR) is one of the best instrumental methods used to detect and identify inorganic functional groups,

Table 2
XRF elemental composition. Values expressed in weight percentage (%). NS = not significant, i.e. value < 2σ (σ = standard error). ND = not detected.

Sample	SiO_2	Al_2O_3	Fe_2O_3	K_2O	TiO_2	Br	MgO	CaO	Na_2O	P_2O_5
L_1	80.93	14.79	1.54	1.02	0.841	0.331	0.248	0.157	NS	0.0551
L_2	76.9	18.08	1.34	1.62	0.875	0.361	0.4	0.0784	0.096	0.0534
L_3	92.47	5.7	0.315	0.665	0.305	0.25	0.081	0.021	0.076	0.0233
L_4	73.69	19.61	1.37	2.31	1.01	1.1	0.455	0.0443	0.142	0.0655
L_5	88.48	7.23	0.431	0.843	0.928	1.35	0.138	0.0552	0.3	0.0383
L_6	66.05	23.41	4.59	2.63	0.967	0.978	0.515	0.254	0.213	0.159
L_7	67.14	24.3	1.88	2.76	0.908	0.28	0.659	0.127	0.251	0.0514
L_8	73.97	19.86	1.88	2.27	0.813	0.275	0.447	0.134	0.123	0.0567
L_9	73.23	19.58	1.5	2.36	0.882	1.4	0.461	0.199	0.165	0.0521
L_10	92.86	4.45	0.834	0.214	0.0518	1.45	ND	0.0251	ND	0.0224

Table 3
Mineralogical content. The percentage of quartz and phyllosilicates are semiquantitatively measured on whole sample. However, the clay-mineral content (fourth and fiftth columns) is related to clay minerals present in the < 2 μm fraction of the oriented aggregates. The sixth column indicates minerals found in the clay < 2 μm fraction.

Sample	Whole rock		<2 μm fraction		
	% Quartz	% Phyllosilicate	% Illite	% Kaolinite	Other minerals
L_1	54	46	5	95	
L_2	49	51	13	87	Goethite
L_3	89	11	5	95	
L_4	65	35	35	65	Jarosite
L_5	80	20	19	81	
L_6	38	62	28	72	
L_7	47	53	26	74	Goethite
L_8	52	48	23	77	Goethite
L_9	64	36	17	83	Goethite
L_10	97	3	1	99	Lepidocrocite

which are characteristic of different minerals. This technique is focused on the vibration modes of molecular and/or polynuclear ionic species contained in both crystalline and non-crystalline compounds. Therefore, the IR has become into a useful tool not only for the identification of mineral compounds, but also to give a qualitative and quantitative insight into the composition of mineral mixtures.

The FT-IR spectra measured on powder samples were registered by the ATR method (Figs. 3 and S.2 – S.6). A comparison among the intensity of the spectra, measured in the same experimental conditions, given in Fig. S.2, clearly revealed that **L_3**, **L_5** and **L_10** showed a weaker intentity than the other samples. Tentative assignments of the bands are provided in Fig. 3 and Table S.3. The absorption about 3690 cm^{-1} was attributed to the ν(Si)O-H mode of hydroxyde groups not involved in hydrogen bonds, strongly coupled with in-phase symmtetric stretch. Bands at 3672, 3665, 3650 and 3615 cm^{-1} were assigned to ν(O-H) vibrations in hydrogensilicate moieties involved in symmetric hydrogen bonds, as (Si)[O-H···OH]$_2$(Si) [36,37]. A weak band at 3389 cm^{-1} only visible in the spectrum of **L_4** strongly resembled that characteristic of jarosite (3390–3375 cm^{-1}) [38] (Fig. S2).

Weak bands in the 1645–1631 cm^{-1} region could be due to bending δ(HOH) modes of water. A tiny absorption at 1417 cm^{-1} in **L_4** was assigned to the $\nu_3(CO_3^{2-})$ vibration of traces of carbonate. The broad and intense band with minimum at 1030–1021 cm^{-1} was actually a complex structure that incorporated different absorptions attributed to stretching ν(Si-O) modes [39,40]. In the case of kaolinite, two well-differenced bands appear about 1033–1028 and 1007–995 cm^{-1}, respectively [40–42]. Muscovites also exhibit analogous bands approximately at 1027 and 1003 cm^{-1} [39].

Bands about 936–932 and 911–910 cm^{-1} were assigned to bending OH vibrations in Al-OH-Al moieties [43–45]. The weak absorption at 830 cm^{-1} could be due to a librational Al-OH mode in muscovite [39].

In the 795–692 cm^{-1} region different bands arose, which were mainly attributed to bending Si-O, Si-O-Si and Si-O-Al modes. In particular, 795 (kaolinite and quartz), 777 (quartz), 752 (kaolinite and muscovite) and 692 cm^{-1} (kaolinite and quartz) [39,41,43,44]. A careful analysis of the maxima and valleys of the absorbance spectra in the 850–710 cm^{-1} region (Fig. 4a) was carried out, which involved a base line correction performed fitting

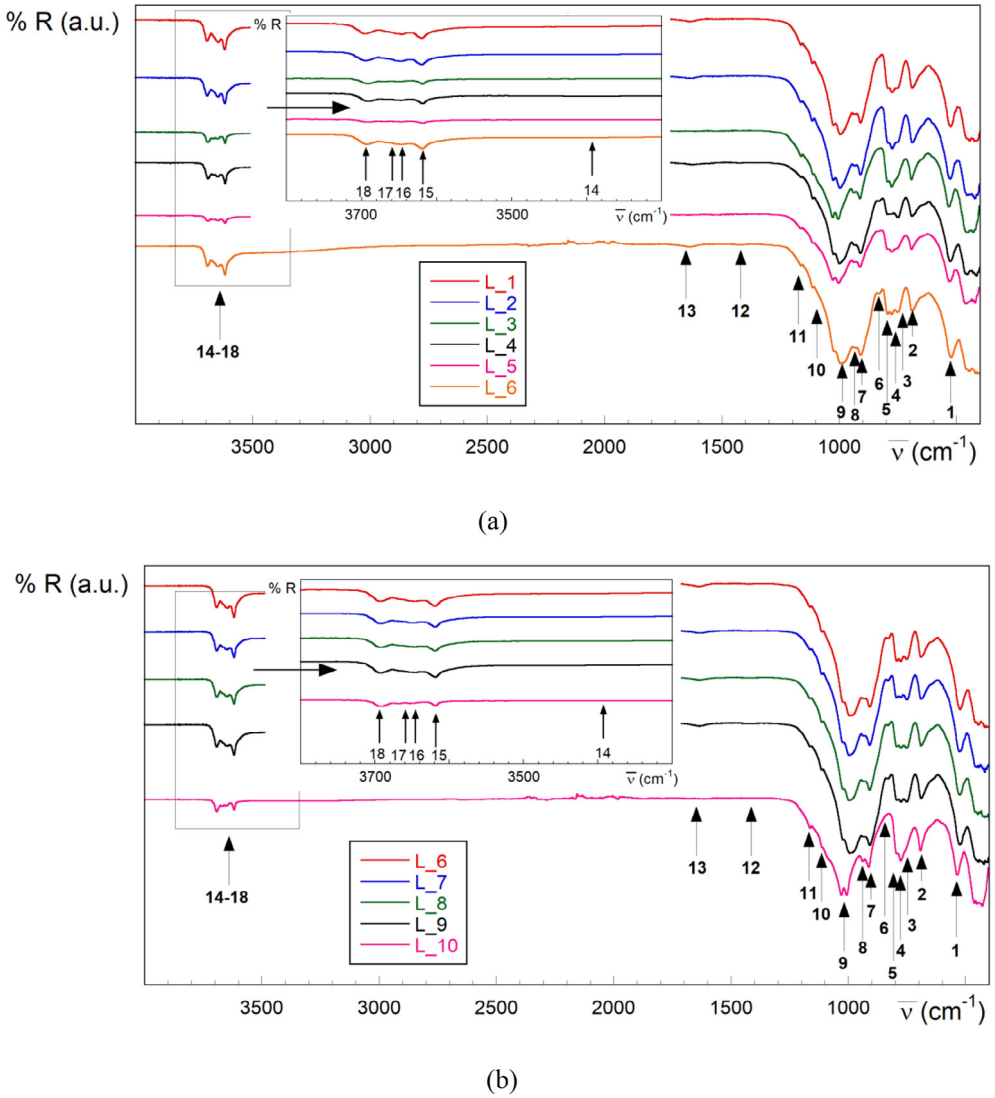

Fig. 3. IR spectra of **L_1** – **L_6** (a) and **L_6** – **L_10** (b) in the 4000–400 cm^{-1} range. Curves in the 3800–3300 cm^{-1} region are zoomed in. Corresponding assignments (see main text): (**1**) δ(Si – O – Si); (**2**) ν_2(Si-O); (**3**) δ(Si – O – Al); (**4**) δ(Si – O – Si); (**5**) δ(Si – O – Si/Al); (**6**) δ(Al – OH)$_{muscovite}$; (**7**) δ(OH)$_{inner\ Al\text{-}OH\text{-}Al}$; (**8**) δ(OH)$_{surface\ Al\text{-}OH\text{-}Al}$; (**9**) ν(Si – O – Si)$_{in\ plane}$; (**10**) ν(SiO)$_{apical\ in\ kaolinite/muscovite}$; (**11**) ν(SiO)$_{apical\ in\ quartz}$; (**12**) $\nu_3(CO_3^{2-})$; (**13**) δ(OH,H_2O); (**14**) ν(OH,H_2O); (**15**) ν(OH)$_{inner\ hydroxide}$; (**16**) ν(OH)$_{inner\text{-}surface}$; (**17**) ν(OH)$_{surface}$; (**18**) $\nu_{(OH)surface}$.

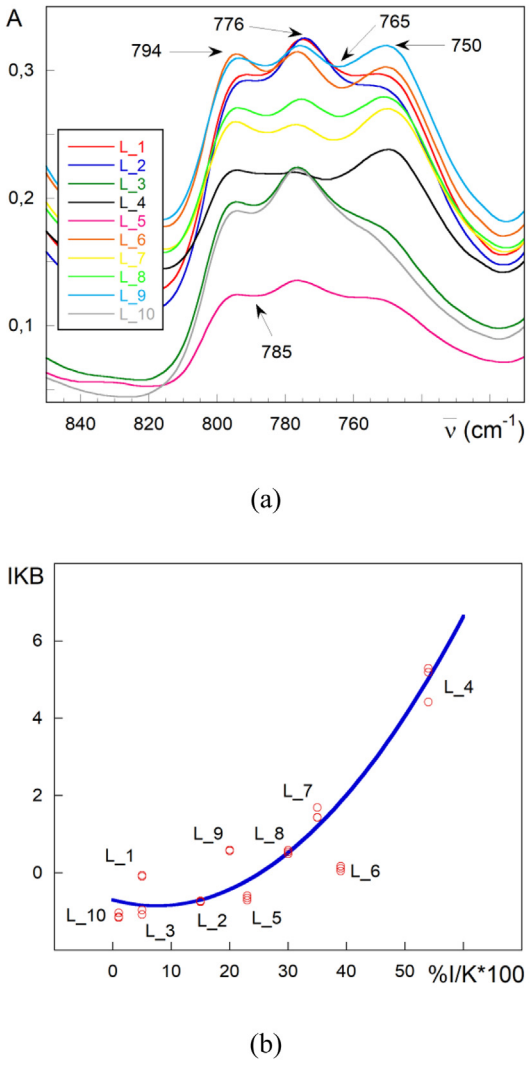

Fig. 4. (a) Selected IR absorbance bands in the 850–710 cm^{-1} region. (b) Plot of IKB *vs* % (I/K)*100, three measurements per sample (circles in red), see text for details.

to zero the minima in absorbance observed around 826–815 and 716–715 cm^{-1}. The absorbance values were selected from the observed maxima and minima wherever possible. Fixed values (Fig. 4a) were considered where reading was not possible. All these data were used to perform an illite/kaolinite band ratio parameter (IKB, Eq. (1)), which was plotted against the illite/kaolinite ratio in the 2 μm fraction of the oriented agregate XRD study (I/K, Fig. 4b). Briefly, muscovite-rich sediments showed large IKB values. The parabolic curve depicted in blue (Fig. 4b, Eq. (2), goodness of fit R = 0.98) was built by fitting the average of three measurements per sample. The most divergent spectra, the **L_6** and **L_9** values, were excluded for the fit. In the case of **L_6**, the IKB value is considerably lower than that predicted in the curve. It reflects a decrease in A_{750} (mainly Si-O-Al) and an increase in A_{794} due to the replacement of aluminium for iron. This observation is in accordance with the contribution of bending Fe-OH and Mg-OH modes to the band at 794 cm^{-1} in illite–smectite mixtures [46]. This fact is in good agreement with the palaeosoil related chemical meteorization depicted by the Fe-rich clay **L_6** sediment, which was sampled from a red palaeosoil (fluvisol) layer. No successful explanation was found for the disagreement in **L_9**. A possibility could be related to uncertainties in the reading of maxima and minima in samples with high kaolinite (>80%) and a medium value of quartz (50–65%) contents. Moreover, slight influences of the grinding time / particle size were observed in the samples (some examples are given in Figs. S.7 and S.8), the greater intensity the longer grinding times together with minor changes in the resolution of bands about 750 and 470 cm^{-1}, in line with studies reported elsewhere [47]. In summary, the IKB parameter seems to be useful to infer the proportion of illite/kaolinite present in clay samples, a relationship that can be controlled, for example, by paleogeographic variables as changes in the source area or climatic conditions [48,49], diagenetical processes [50], hydrothermal activity [51] or industrial processes [52]. The presence of outliers in the IKB graphic could provide a fast graphical insight for the substitution of Al (III) by Fe(III) ions in certain illite/kaolinite mixtures, as is the case of the sample **L_6**.

$$IKB = \frac{(A_{750} - A_{765}) - (A_{794} - A_{785})}{(A_{776} - A_{765})} \quad (1)$$

$$IKB_{Fit} = -0.69609 - \left(0.040745 \times \frac{I}{K}\right) + \left[0.002717 \times \left(\frac{I}{K}\right)^2\right] \quad (2)$$

Finally, the absorptions about 535–523 cm^{-1} were mainly attributed to δ(Si-O-Si) modes [37].

3.3.2. UV–vis

Variations in the ultraviolet–visible (UV–vis) absorption spectra of the sediments can denote differences in the chemical contents or grain sizes. The UV–vis measurements were registered on powdered solid samples by diffuse reflectance technique (Figs. S.9 and S.10, Table S.4). Two bands appeared at 235–240 and 260 nm in all the samples, except for **L_10**, which could be attributed to O → Fe(III) charge transfer bands involving octahedral Fe (III) ions substituting for Al(III) and Mg(II) ions, respectively [53]. The most of the samples exhibited a broad shoulder around 485 nm. This absorption could not be distinguish for **L_1** and **L_4** and, in the case of the red **L_6** sample, this shoulder shifted to 535 nm and was assigned to a forbidden $^6A_1(S) \rightarrow {}^4T_{2g}(G)$ d-d transition in muscovite [54], in good agreement with the presence of a greater amount of Fe(III) ions [55,56].

3.3.3. EPR

The existence of paramagnetic species, as transition metal ions and organic or inorganic radicals, can be detected by electron paramagnetic resonance (EPR). This technique provides information about the nature of the paramagnetic centers and their geometrical (metal ions) and topological (radicals) environments. Three features could be distinghised in the EPR spectra of all the analyzed sediments at RT (Fig. 5): (a) a signal at $g \sim 4$, placed over a plateau or tail spread between 60 and 113 mT; (b) a very broad absorption at $g \sim 2$; and (c) one or several thin and usually intense radical signals about $g = 2$ (Fig. 5 (c)). The spectra strongly resembled those reported in the Literature for kaolinite and analogous minerals, as dickite [57–60] or halloysite [61], and also in sudoite [62]. However, the absorption at $g \sim 4$ has been described not only for kaolinite [63], but also for illite [64], muscovite [65], montmorillonite [66] and sepiolite [67]. In the case of the broad signal at $g \sim 2$ is also characteristic of different mica-type minerals as phlogopite and pyrophillite [68], or brasilian [69] and australian muscovites [70].

Different signals appeared at low magnetic field with g–values about 5.00, 4.16 and 3.52 and an unresolved plateau-like tail at $g \sim 9$, being the most intense that at $g = 4.16$. No variations were observed upon decreasing the temperature to 120 K, except for the increase in the amplitude (Figs. S.11 and S.12). All these features could be attributed to high spin Fe(III) ions (d^5, S = 5/2) placed in isolated distorted octahedral sites [71,72]. The presence of these signals in kaolinites, illites and related minerals is

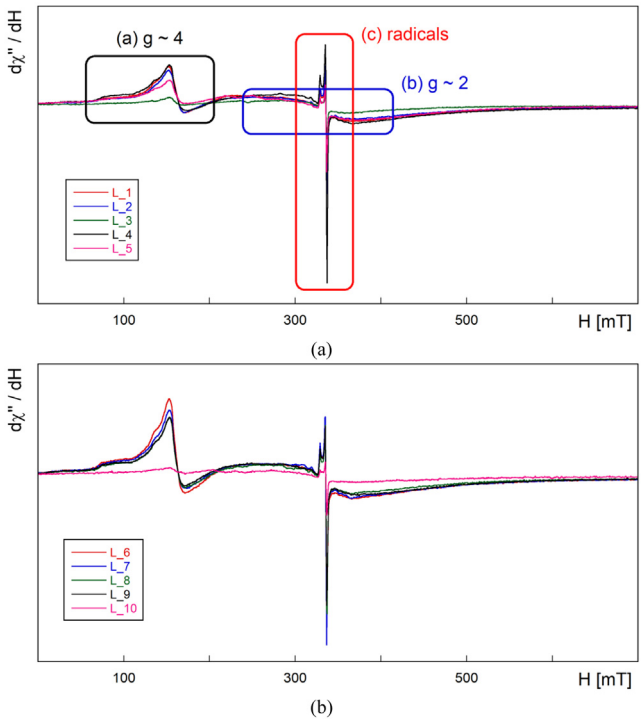

Fig. 5. EPR spectra at RT of **L_1** – **L_5** (a) and **L_6** – **L_10** (b) in the 0–700 mT range. The three absorptions characteristic of the spectra, as discussed in text, are depicted in Figure (a). Experimental details: microwave frequency 9.42 GHz, modulation amplitude 0.1 mT, time constant 40.96 ms, conversion time 81.92 ms, receiver gain 6.32 10^4, power 20 mW, modulation frequency 100 kHz.

attributed to the partial replacement of Al(III) ions by Fe(III) ones in the two kinds of octahedra that exist in the crystal structure of the mineral [73–76]. In fact, two kind of signals are distinguished in this region: (i) an isotropic line at g = 4.2, described in the Literature with the name of Center I [77,78]; (ii) other lines with g–values 9, 4.9, 3.7 and 3.5, labelled as Centers IIa and IIb [58]. Center I is ascribed to orthorhombic sites radomly distributed, while Center II are associated to highly crystalline domains or regular stacking [79,80]. In adition, the intensity of signals in this region increases with the Fe(III) content in clays [81,82], except for high iron amounts (greater than 30% w/w in Fe_2O_3), in these cases the trend is inverted [83]. In our spectra, the largest signal corresponded to the Center I one in **L_6**, which exhibited a substitution degree close to 16% at the most. The predominance of Center I in our samples clearly indicated the destruction in the regular pattern of the replacement of Al(III) by Fe(III) ions [84].

Regarding the broad isotropic signal at $g \sim 2$, a reasonable fit was achieved in our spectra considering g = 2.06 and a line width $\triangle H$ = 80 mT. This absorption could be attributed to the presence of magnetic coupling in Fe–O–Fe moieties of iron-rich mineral impurities of kaolinite [85,86], as iron basic oxides on the clay surface [87–89]. The XRD results showed that some of our samples contained goethite ($_\alpha$-FeOOH, Table 3), despite the presence of this mineral in the other sediments could be undetectable by XRD due to its low crystallinity [90]. The relative low intensity of this line in our samples suggested the existence of little ferric oxide amounts in them.

A magnification of the main radical signal for the spectrum of **L_7** at RT is shown in Fig. 6 (a), together with its best fit. The calculated g-values hardly varied for the rest of the samples (Table S.5, Fig. S.13), and the following average parameters for this chromophore could be obtained: g_x = 2.0026(2), g_y = 2.0082(2) and g_z = 2.0503(2). Notwithstanding, the g_y value exhibited a larger

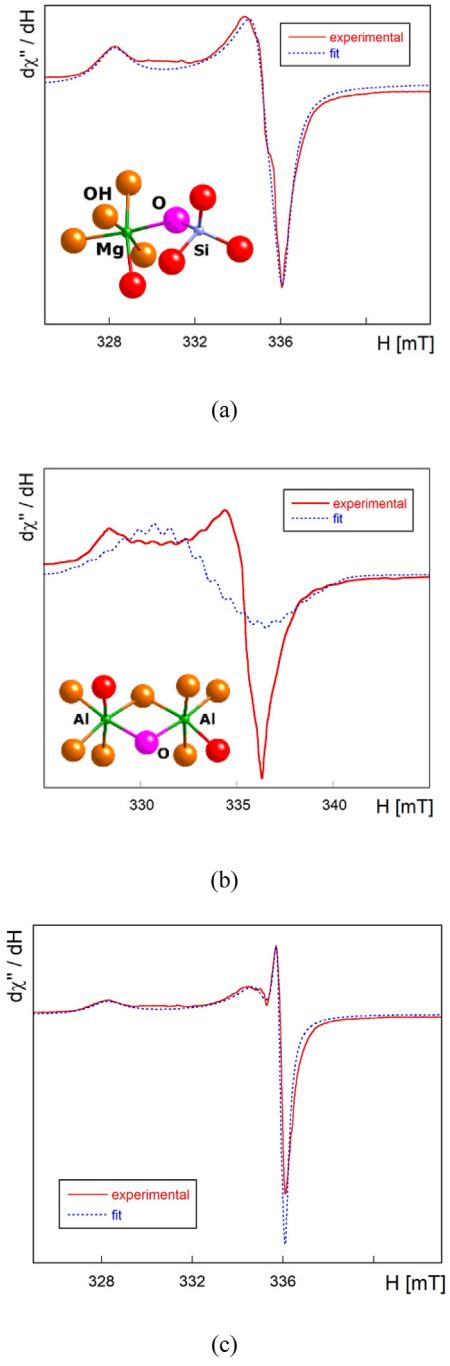

Fig. 6. EPR spectra (continuous red lines) and their best fits (dotted blue lines) for: (a) **L_7** at RT, with drawing of A-Center inset, with the oxygen atom with electron vacant in pink; (b) **L_7** at 120 K, with drawing of B-Center inset, and (c) **L_4** at RT. Atom colors: yellow (hydroxide O atom), red (O), green (Al, Mg), light blue (Si). Experimental and fitting details are given as footnotes.Experimental and fitting details:(a) RT, microwave frequency 9.4187 GHz, modulation amplitude 0.1 mT, time constant 81.92 ms, conversion time 327.68 ms, receiver gain 6.32 10^4, power 20 mW, modulation frequency 100 kHz. Fit: Lorentzian-type signal, g_1 = 2.0024 ($\triangle H_1$ = 0.60 mT), g_2 = 2.0080 ($\triangle H_2$ = 0.90 mT) y g_3 = 2.0504 ($\triangle H_3$ = 1.20 mT).(b) RT, microwave frequency 9.4187 GHz, modulation amplitude 0.1 mT, time constant 81.92 ms, conversion time 327.68 ms, receiver gain 6.32 10^4, power 20 mW, modulation frequency 100 kHz. Fit: Lorentzian-type signal, g_1 = 2.0008 ($\triangle H_1$ = 0.50 mT), g_2 = 2.0200 ($\triangle H_2$ = 0.50 mT) y g_3 = 2.0360 ($\triangle H_3$ = 0.50 mT), A_1 = 6.72 10^{-4} cm^{-1} (0.72 mT), A_2 = 7.26 10^{-4} cm^{-1} (0.77 mT) y A_3 = 7.98 10^{-4} cm^{-1} (0.84 mT).(c) RT, the same parameters given in (a), except for microwave frequency 9.4186 GHz and power 2 mW. The fit was achieved from adition of two Lorentzian signals attributed to the A-Center (i) and the organic radical (ii), respectively. (i) g_1 = 2.0023 ($\triangle H_1$ = 0.18 mT), g_2 = 2.0082 ($\triangle H_2$ = 0.80 mT) y g_3 = 2.0502 ($\triangle H_3$ = 1.00 mT); (ii) g = 2.0036 and $\triangle H$ = 0.30 mT. B-Center contribution has not been considered in the fit.

uncentainty because the fit was not completely achieved due to the overlapping with another non well-resolved hyperfine structure laying between 329 and 332 mT. This radical signal did not show relevant changes upon lowering the temperature to 120 K, except for **L_3**, **L_5**, and **L_10** (Fig. S.14, Table S.6), and the obtained values agreed well with those published from Q-band EPR studies on the kaolinite A-Center, g_x = 2.001, g_y = 2.006 y g_z = 2.049 [91]. This signal is attributed to an electronic vacant on the π-orbital of an oxygen atom in a Si–O bond, associated to defects of the oxygen atoms linking the octahedra and tetrahedra sheets, where Al(III) ions in octahedra could be partially replaced by Mg(II) ions, Fig. 6 (a) inset [6,91,92]. The A-Center is quite stable, its formation is induced by any kind of radiation, as α, β, or γ-rays and nuclear recoil [93].

A hyperfine structure formed a plateau in the 329.5–332.5 mT region, whose resolution clearly increased on lowering temperature, and was attributed to the B-Center in kaolinites. The *g*-values of the tentative fit depicted in Fig. 6 (b) for **L_7** at 120 K agreed well with those reported in the Literature for this signal, g_x = 2.002, g_y = 2.020 y g_z = 2.040, A_x = 6.76 10^{-4} cm^{-1} (0.71 mT), A_y = 7.26 10^{-4} cm^{-1} (0.77 mT) and A_z = 6.85 10^{-4} cm^{-1} (0.84 mT) [94]. B-Center is proposed to be formed in kaolinites and dickites as a result of the hole provoked by an incident radiation on an oxygen atom placed between two Al(III) ions, with formation of O- [92,95], Fig. 6 (b). The resolution by narrowing of the signals of the B-Center provoked a distortion of the weakest A-Center signals, i.e. those corresponding to **L_3**, **L_5** and **L_10** (see Fig. S.15 (a,b)).

The **L_4** sample, and in a lesser extent **L_8**, showed the presence of an isotropic radical signal, overlapped with those of A- and B-Centers, with estimated *g* = 2.0036(7) and line width $\triangle H$ = 0.30 mT (Figs. 5 (c) and S.16). This signal resembled that obtained after treatment of kaolinites with oxalic acid [43]. The position and line width suggested this signal could be due to organic free radicals, as those found in Brazilian oil shale byproduct samples [96], lignite-kaolinite system [97], humic acids of goethite-rich sediments [98], or carbonaceous materials [99], as lignite [100] or bituminous coals [101]. The signals in them have been attributed to defects in the electon structure of the carbon atoms, such as dangling bonds with unpaired electrons in the edges of the graphene sheets [99], or carbon-centered radicals adjacents to oxygen atoms [101–103]. However, other posibilities for explaining the origin of the absorption in our samples cannot be completely ruled out, as the presence of SO_3- radicals as those with *g* = 2.0028–2.0042 reported in mineral sulfates [104], despite it is unlike because no appreciable sulfur content was detected in the analyses of **L_8**.

Finally, a comparison among the intensities of the different EPR signals was carried out acording to the method and parameters described in Supporting Information (Fig. S.17 and Tables S.7 and S.8). In this way, the **L_6** sample exhibited the greatest values for the integral and peak-to-peak amplitude of the signal at $g \sim 4$ (S.4 and $\triangle I_{g\sim4}$), together with low values for the parameters with $\triangle I_{g\sim4}$ as denominator, which suggested **L_6** contained the greatest amount of Fe(III) ions in distorted geometries replacing Al(III) ions. On the other hand, the most intense A-Center radical signals nicely correlated with the MgO content (Tables S.1 and values of S_{23} in Table S.7), except for the **L_4** sample due to the overlapping with the organic radical absorptions, in good agreement with the origin of the A-Center signal in Mg – O – Si moieties. Anyway, all the studied samples with intense radical signals had high uranium, thorium and postassium-contents, see Tables 2 and S.2 (a and c), whose natural radionuclides represent one of the main sources of defects formation [105].

In summary, the ten EPR spectra exhibited important analogies and its mineral origin was, essentially, kaolinite and illite (muscovite), except for the intense isotropic signal in **L_4** attributed to organic radicals. The intensities of the spectra of **L_3**, **L_5** and **L_10** were very weak, in accordance with a low phyllosilicate content. **L_6** was the sample with the highest amount of Fe(III) replacing Al(III) ions in clays.

3.4. Antioxidant ability of the sediments

The antioxidant capacity of a compound depends, at least in part, on the ability to quench radicals or reactive oxygen species. Different complementary methods are used to evaluate the antioxidant activity of complex extracts, due to the great variety of mechanisms involved. The most commonly applied methodologies are based on the capacity to evaluate the reducing ability of antioxidants, the scavenging of stable radicals or the scavenging of peroxyl radicals.

The present work focused on the ABTS and DPPH methods and the lipid peroxyl scavenger capacity LPSC method. Q-ABTS measures the antioxidant capacity as the ability of an antioxidant compound to decrase ABTS color (band at 734 nm) by reacting directly with the ABTS and quenching the radical by electron transfer. The ABTS radical was generated in high yield using potassium persulfate as the oxidizing agent. Q- DPPH is a stable radical with a deep purple color, whose reaction with antioxidant compounds provokes a loss of color at 517 nm. In contrast to water-soluble ABTS, DPPH is hydrophobic so its reactions were performed in organic solvents.

3.4.1. Total antioxidant capacity

The ability of the studied raw clays to act as scavengers of the ABTS radical was analyzed and the results were expressed as trolox-equivalents. The results indicated a higher antioxidant ability for **L_6**, **L_7**, **L_8** and **L_9** (Fig. 7). In the opposite, **L_3** and **L_10** showed the lowest antioxidant properties. Analogous results arose from the DPPH assay, but in this case differences in the antioxidant capacity of the sediments were lower, except for the extreme values (i.e. **L_6** *vs.* **L_3**/**L_10**). Note that the sediments with the highest antioxidant activity were rich in non-organic hydrogen and orthorhombic Fe(III) ions replacing Al(III) ones in distorted octahedral positions (Table S.7).

Furthermore, with the aim to check if the source of the antioxidant activity was the total amount of iron in the samples, the effect of the ferric minerals present in the sediments and a common soluble Fe(III) salt was evaluated. The antioxidant capacities of pure FeO(OH) goethite, Fe_2O_3 hematite and $FeCl_3$ measured by the Q-ABTS method were 47.7 ± 15.3, 124 ± 11.9 and 46.7 ± 4.9 nmoleq trolox/g sediment, respectively. These values were low with respect to those measured in the sediments with a higher antioxidant capacity. The assays of these three compounds by the Q-DPPH method yielded not detectable antioxidant capacity. Therefore, the presence of soluble Fe(III) species, or Fe(III)-containing minerals as goethite and hematite, seem not to be the main responsible, at least by itself, of the reactivity against radicals found for the studied sediments in the described experimental conditions. In spite of other possibilities could be considered, as synergic effects among the components of the sediments including these ferric oxide minerals, our results strongly suggested that samples with the highest scavenging activity were those whose clay minerals presented the greatest amount of Fe(III) replacing Al(III) ions.

The antioxidant capacity in clays has been evaluated by other authors in systems as halloysite [19], thermal mud [22], montmorillonite [106], metallic iron-containing kaolinites [107,108], and other natural clays [109,110].

The capacity of the sediment samples to inhibit lipid peroxidation was evaluated by Q-LPSC method. Preliminary results showed that all the compounds had antilipidperoxidation activity with a

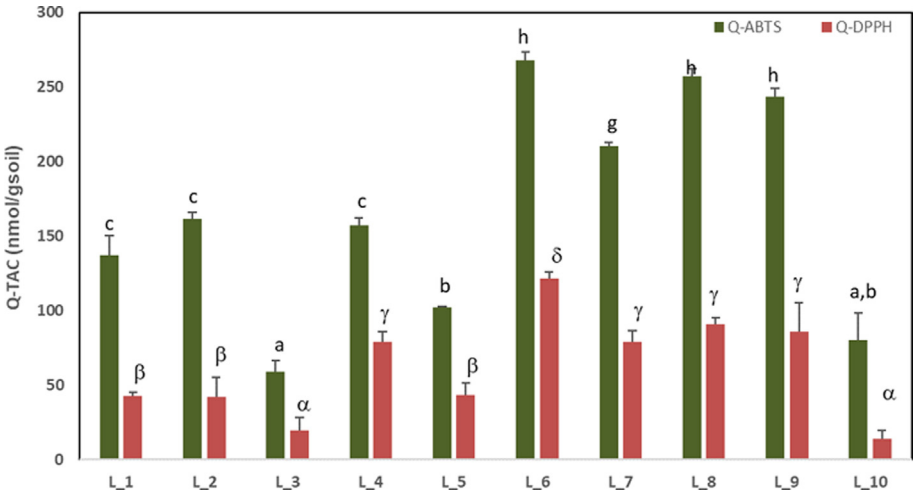

Fig. 7. Quencher total antioxidant capacity (Q-TAC) of the studied sediments. TAC: Total antioxidant capacity expressed as nmol equiv Trolox/g sediment. Data expressed as mean values of standard deviation (n = 3). Latin and greek letters indicate significant differences among the studied sediments evaluated by Q-ABTS and Q-DPPH respectively.

capacity close to 50% and no significant differences among the samples (Fig. S.18).

4. Conclusions

As far as we are aware, the work here described represents the first mid-infrared, EPR and antioxidant study carried out on sediments coming from the Utrillas Formation, a geological sequence in the Iberian Peninsula paradigmatic and relevant for the economic, historic and palaeontological richness (sauropod remains, quarries, minering...). The analyzed sediments exhibited similar spectroscopic but distinct analytic features. They were mainly formed by three polycrystalline minerals, in different amounts: quartz, muscovite and kaolinite. The combination of instrumental techniques allowed a deep study of kaolinite, which incorporated inorganic radicals related to defects in oxygen atoms in different environments. The intensities of the radical signals agreed well with the Mg, U, Th and K contents in the corresponding sediments. An organic radical was also detected in the sediment with a major carbon content, **L_4**. A new FTIR band ratio parameter, IKB, was defined and seemed to vary depending on the illite/kaolinite ratio in the clay samples, which could be potentially applied to different clay sediment research lines. This parameter, together with UV–visible and EPR methods, provided tools to evaluate the substitution of aluminium for iron in the clays, which appeared to be related to the activity of these sediments as scanvengers of the ABTS and DPPH radicals, the more active the richer in iron that replaces aluminum. Preliminary studies showed slight inhibition of lipid peroxidation by all these sediments.

CRediT authorship contribution statement

Javier García-Tojal and **Eneko Iriarte:** Conceptualization, Methodology, Validation, Investigation, Resources, Writing - original draft. **Susana Palmero:** Investigation, Resources. **María R. Pedrosa:** Funding acquisition, Supervision. **Carlos Rad:** Investigation, Resources, Methodology, Supervision. **Silvia Sanllorente:** Investigation, Resources. **María Cruz Zuluaga:** Conceptualization, Methodology, Supervision. **Mónica Cavia-Saiz:** Investigation. **Dolores Rivero-Perez:** Investigation. **Pilar Muñiz:** Investigation, Resources, Methodology, Supervision.

Declaration of Competing Interest

The authors declare that they have no known competing financial interests or personal relationships that could have appeared to influence the work reported in this paper.

Acknowledgement

We are very grateful to Borja Rosales, and the Asociación para el Desarrollo de Tierra de Lara, for enticing us with questions and proposals, which gave rise to the research here described. We also thank Dr. J. J. Delgado, Dr. Pilar Castroviejo, Marta Mansilla, Dr. Ana Erica Páramo and Zaida Cabello (PCT, Universidad de Burgos, Spain) for the elemental, XRF and XRD analyses, and Francisco Javier Sangüesa (Advanced Research Facilities, SGIker, of the University of the Basque Country, UPV/EHU) for the oriented aggregates study. This work was supported by Consejería de Educación of Junta de Castilla y León BU022G18, Junta de Castilla y León and FEDER BU291P18 and BU049P20, Ministerio de Economía y Competitividad CTQ2016-75023-C2-1-P and Ministerio de Ciencia, Innovación y Universidades CTQ(QMC) RED2018-102471-T MultiMetDrugs Network (Spain).

Appendix A. Supplementary material

FT-IR, UV-vis and EPR spectra and the assignments are provided in Figs. S.1–S.18 and Tables S.1–S.8. Supplementary data to this article can be found online at https://doi.org/10.1016/j.saa.2021.119472.

References

[1] H.G. Dill, Kaolin: Soil, rock and ore: From the mineral to the magmatic, sedimentary and metamorphic environments, Earth-Sci. Rev. 161 (2016) 16–129.
[2] H.H. Murray, Overview - clay mineral applications, Appl. Clay Sci. 5 (1991) 379–395.
[3] H.H. Murray, Major Kaolin Processing Developments, Int. J. Miner. Process. 7 (1980) 263–274.
[4] H.H. Murray, Traditional and new applications for kaolin, smectite, and palygorskite: A general overview, Appl. Clay Sci. 17 (2000) 207–221.
[5] J. Ortiz, M. Montaño, A. Plascencia, J. Salinas, Influence of kaolinite clay supplementation on growth performance and digestive function in finishing calf-fed holstein steers, Asian Australas. J. Anim. Sci. 29 (2016) 1569–1575.
[6] N. Worasith, B.A. Goodman, Influence of particle size on the paramagnetic components of kaolins from different origins, Clay Miner. 47 (2012) 539–557.

[7] M. Romanelli, F. Di Benedetto, G. Fornaciai, M. Innocenti, G. Montegrossi, L.A. Pardi, A. Zoleo, F. Capacci, ESEEM of industrial silica-bearing powders: reactivity of defects during wet processing in the ceramics production, Phys. Chem. Miner. 42 (2015) 363–372.

[8] M.S. Prasad, K.J. Reid, H.H. Murray, Kaolin: processing, properties and applications, Appl. Clay Sci. 6 (1991) 87–119.

[9] López-Galindo, Viseras, C. Pharmaceutical and cosmetic applications of clays. In Wypych, F., Satyanarayana, K.G., Eds., 2004, Clay sufaces. Fundamentals and applications, Elsevier Academic Press, Amsterdam.

[10] M.I. Carretero, M. Pozo, Clay and non-clay minerals in the pharmaceutical industry. Part I. Excipients and medical applications, Appl. Clay Sci. 46 (2009) 73–80.

[11] C. Gomes, M.I. Carretero, M. Pozo, F. Maraver, P. Cantista, F. Armijo, J.L. Legido, F. Teixeira, M. Rautureau, R. Delgado, Peloids and pelotherapy: Historical evolution, classification and glossary, Appl. Clay Sci. 75–76 (2013) 28–38.

[12] F. Armijo, F. Maraver, M.I. Carretero, M. Pozo, M. Ramos, M.A. Fernandez-Torán, I. Corvillo, The water effect on instrumental hardness and adhesiveness of clay mixtures for pelotherapy, Appl. Clay Sci. 114 (2015) 395–401.

[13] J. Cervini-Silva, A. Nieto-Camacho, V. Gómez-Vidales, S. Kaufhold, B.K.G. Theng, The anti-inflammatory activity of natural allophane, Appl. Clay Sci. 105–106 (2015) 48–51.

[14] F. Kang, Y. Ge, X. Hu, C. Goikavi, M.G. Waigi, Y. Gao, W. Ling, Understanding the sorption mechanisms of aflatoxin B1 to kaolinite, illite, and smectite clays via a comparative computational study, J. Hazard. Mater. 320 (2016) 80–87.

[15] M.I. Carretero, M. Pozo, J.L. Legido, M.V. Fernández-González, R. Delgado, I. Gómez, F. Armijo, F. Maraver, Assessment of three Spanish clays for their use in pelotherapy, Appl. Clay Sci. 99 (2014) 131–143.

[16] M.E. Awad, A. López-Galindo, M. Setti, M.M. El-Rahmany, C.V. Iborra, Kaolinite in pharmaceutics and biomedicine, Int. J. Pharm. 533 (2017) 34–48.

[17] S. Sadri, B.B. Johnson, M. Ruyter-Hooley, M.J. Angove, The adsorption of nortriptyline on montmorillonite, kaolinite and gibbsite, Appl. Clay Sci. 165 (2018) 64–70.

[18] A. Septian, S. Oh, W.S. Shin, Sorption of antibiotics onto montmorillonite and kaolinite: competition modelling, Environ. Technol. (United Kingdom) 40 (2019) 2940–2953.

[19] H. Cornejo-Garrido, A. Nieto-Camacho, V. Gómez-Vidales, M.T. Ramírez-Apan, P. del Angel, J.A. Montoya, M. Domínguez-López, D. Kibanova, J. Cervini-Silva, The anti-inflammatory properties of halloysite, Appl. Clay Sci. 57 (2012) 10–16.

[20] J. Cervini-Silva, A. Nieto-Camacho, M.T. Ramirez-Apan, V. Gomez-Vidales, E. Palacios, A. Montoya, E. Ronquillo de Jesus, Anti-inflammatory, anti-bacterial, and cytotoxic activity of fibrous clays, Colloids Surf. B Biointerfaces 129 (2015) 1–6.

[21] J. Cervini-Silva, A. Nieto-Camacho, V. Gómez-Vidales, Oxidative stress inhibition and oxidant activity by fibrous clays, Colloids Surf. B Biointerfaces 133 (2015) 32–35.

[22] M. Centini, M.R. Tredici, N. Biondi, A. Buonocore, R. Maffei Facino, C. Anselmi, Thermal mud maturation: Organic matter and biological activity, Int. J. Cosmet. Sci. 37 (2015) 339–347.

[23] M.I. Carretero, Clay minerals and their beneficial effects upon human health. A review, Appl. Clay Sci. 21 (2002) 155–163.

[24] M.E. Awad, A. López-Galindo, M.M. El-Rahmany, H.M. El-Desoky, C. Viseras, Characterization of Egyptian kaolins for health-care uses, Appl. Clay Sci. 135 (2017) 176–189.

[25] W. Ding, Y. Wang, Y. Yu, X. Zhang, J. Li, F. Wu, Photooxidation of arsenic(III) to arsenic(V) on the surface of kaolinite clay, J. Environ. Sci. (China) 36 (2015) 29–37.

[26] M.J. Aguilar, J. Ramírez del Pozo, O. Riba, Algunas precisiones sobre la sedimentación y paleoecología del Cretácico Inferior de la zona de Utrillas-Villarroya de los Pinares (Teruel), Estud. Geol. 27 (1971) 497–512.

[27] J. Arostegui, M.J. Irabien, F. Nieto, J. Sanguesa, M.C. Zuluaga, Microtextures and the origin of muscovite-kaolinite intergrowths in sandstones of the Utrillas Formation, Basque Cantabrian Basin, Spain. Clays Clay Miner. 49 (2001) 529–539.

[28] EVE, 2009. Mapa de rocas y minerales industriales de la Cuenca Vasco-Cantábrica esc. 1:200.000. Ente Vasco de la Energía e Instituto Geológico y Minero de España. http://info.igme.es/cartografiadigital/geologica/mapa.aspx?parent=../tematica/proyectos.aspx&Id=29&intranet=true&language=es#mapas (accessed 31.08.2020)

[29] V. Alonso de Linaje, S.D. Khan, Mapping of diagenetic processes in sandstones using imaging spectroscopy: A case study of the Utrillas Formation, Burgos, Spain. Sediment. Geol. 353 (2017) 114–124.

[30] IGME, 1978b. Hoja n°. 277 Salas de los Infantes. Mapa Geológico de España E. 1:50.000. Instituto Geológico y Minero de España, 2ª ser., 1ª ed., 34 pp. y 1 map. Madrid, Spain.

[31] L.G. Schulz, 4. Quantitative interpretation ofmineralogical composition from X-ray and chemicaldata for the pierre shale, Geol. Survey Prof. Paper 391 – C 31 (1964) pp.

[32] P.E. Biscaye, Mineralogy and sedimentation ofrecent deep-sea clay in the Atlantic Ocean andadjacent seas and oceans, Geol. Soc. Am. Bull. 76 (1965) 803–832.

[33] Barahona, E. Arcillas de ladrillería de la provincia de Granada. Evaluación de algunos ensayos de materias primas, PhD thesis, Univ. Granada, Spain, 1974.

[34] R. Del Pino-García, J. García-Lomillo, M.D. Rivero-Pérez, M.L. González-SanJosé, P. Muñiz, Adaptation and validation of QUick, Easy, New, CHeap, and Reproducible (QUENCHER) Antioxidant Capacity Assays in Model Products Obtained from Residual Wine Pomace, J. Agric. Food Chem. 63 (2015) 6922–6931.

[35] M. Cavia-Saiz, M.D. Busto, M.C. Pilar-Izquierdo, N. Ortega, M. Perez-Mateos, P. Muñiz, Antioxidant properties, radical scavenging activity and biomolecule protection capacity of flavonoid naringenin and its glycoside naringin: a comparative study, J. Sci. Food Agric. 90 (2010) 1238–1244.

[36] A.M. Efimov, V.G. Pogareva, IR absorption spectra of vitreous silica and silicate glasses: The nature of bands in the 1300 to 5000 cm^{-1} region, Chem. Geol. 229 (2006) 198–217.

[37] A. Táborosi, R.K. Szilagyi, B. Zsirka, O. Fónagy, E. Horváth, J. Kristóf, Molecular treatment of nano-kaolinite generations, Inorg. Chem. 57 (2018) 7151–7167.

[38] N.V. Chukanov, Infrared Spectra of Mineral Species, Springer International Publishing, Dordrecht, 2014.

[39] B. Velde, Infrared spectra of synthetic micas in the series muscovite-MgAl celadonite, Am. Mineral. 63 (1978) 343–349.

[40] K. Shahverdi-Shahraki, T. Ghosh, K. Mahajan, A. Ajji, P.J. Carreau, Effect of dry grinding on chemically modified kaolin, Appl. Clay Sci. 105–106 (2015) 100–106.

[41] N.J. Saikia, D.J. Bharali, P. Sengupta, D. Bordoloi, R.L. Goswamee, P.C. Saikia, P. C. Borthakur, Characterization, beneficiation and utilization of a kaolinite clay from Assam, India, Appl. Clay Sci. 24 (2003) 93–103.

[42] C. Fourdrin, E. Balan, T. Allard, C. Boukari, G. Calas, Induced modifications of kaolinite under ionizing radiation: An infrared spectroscopic study, Phys. Chem. Miner. 36 (2009) 291–299.

[43] N. Worasith, B.A. Goodman, J. Neampan, N. Jeyachoke, P. Thiravetyan, Characterization of modified kaolin from the Ranong deposit Thailand by XRD, XRF, SEM, FTIR and EPR techniques, Clay Miner. 46 (2011) 539–559.

[44] B.J. Saikia, Spectroscopic estimation of geometrical structure elucidation in natural SiO_2 crystal, J. Mater. Phys. Chem. 2 (2014) 28–33.

[45] A.K. Chakraborty, Phase transformation of kaolinite clay, Springer, New Delhi, 2014.

[46] N.I. Alvarez Acevedo, M.C.G. Rocha, L.C. Bertolino, Mineralogical characterization of natural clays from Brazilian Southeast region for industrial applications, Ceramica 63 (2017) 253–262.

[47] E. Makó, R.L. Frost, J. Kristóf, E. Horváth, The effect of quartz content on the mechanochemical activation of kaolinite, J. Colloid Interface Sci. 244 (2001) 359–364.

[48] S. Caquineau, A. Gaudichet, L. Gomes, M.C. Margonthier, B. Chatenet, Saharan dust: Clay ratio as a relevant tracer to assess the origin of soil-derived aerosols, Geophys. Res. Lett. 25 (1998) 983–986.

[49] F. Ruiz, M. Pozo, M.I. Carretero, J.M. Muñoz, M.L. González-Regalado, M. Abad, T. Izquierdo, J. Rodríguez Vidal, L.M. Cáceres, G. Monge, Whole-rock and clay mineralogy as paleoenvironmental tracers during the Late Holocene sedimentary evolution of the Doñana National Park (SW Spain), Appl. Clay Sci. 197 (2020), 105780.

[50] M. Shaldybin, Y.M. Lopushnyak, I.V. Goncharov, M.J. Wilson, L. Wilson, B.G. Mendis, The mineralogy of the clayey-silty siliceous rocks in the Bazhenov Shale Formation (Upper Jurassic) in the west Siberian Basin, Russia: The role of diagenesis and possible implications for their exploitation as an unconventional hydrocarbon reservoir, Appl. Clay Sci. 136 (2017) 75–89.

[51] A. Aras, The change of phase composition in kaolinite- and illite-rich clay-based ceramic bodies, Appl. Clay Sci. 24 (2004) 257–269.

[52] M. Bentabol, M.D. Ruiz, F.J. Huertas, J. Linares, Chemical and structural variability of illitic phases formed from kaolinite in hydrothermal conditions, Appl. Clay Sci. 32 (2006) 111–124.

[53] R.A. Schoonheydt, Ultraviolet and visible light spectroscopy, Dev. Sedimentol. 34 (1982) 163–189.

[54] B.G.W. Karickhoff, S. Wkarickhoff, Optical absortion spectral a of clay minerals, Clays Clay Miner. 21 (1973) 59–70.

[55] R.A.V. Rossel, R.N. Mcglynn, A.B. Mcbratney, Determining the composition of mineral-organic mixes using UV – vis – NIR diffuse reflectance spectroscopy, Geoderma 137 (2006) 70–82.

[56] Z. Szalai, K. Kiss, G. Jakab, P. Sipos, B. Belucz, The use of UV-VIS-NIR reflectance spectroscopy to identify iron, Astron. Nachrichten 334 (2013) 940–943.

[57] P.J. Malden, R.E. Meads, Substitution by Iron in Kaolinite, Nature 215 (1967) 844–846.

[58] P. Hall, The application of electron spin resonance spectroscopy to studies of clay minerals: I. Isomorphous substitutions and external surface properties, Clay Miner. 15 (1980) 321–335.

[59] J. Komusinski, L. Stoch, S. Dubiel, Application of electron paramagnetic resonance and Mossbauer spectroscopy in the investigation of kaolinite-group minerals, Clays Clay Miner. 29 (1981) 23–30.

[60] J. Götze, M. Plötze, T. Götte, R.D. Neuser, D.K. Richter, Cathodoluminescence (CL) and electron paramagnetic resonance (EPR) studies of clay minerals, Mineral. Petrol. 76 (2002) 195–212.

[61] N. Chaikum, R.M. Carr, Electron spin resonance studies of halloysites, Clay Miner. 22 (1987) 287–296.

[62] É. Morichon, T. Allard, D. Beaufort, D. Quirt, An EPR study of native radiation-induced paramagnetic defects in sudoite (di-trioctahedral Al-Mg chlorite) from the alteration halo related to unconformity-type uranium deposits. Phys. Chem. Miner. 37 (2010) 145–152.

[63] F. Elsass, D. Olivier, Infra red and electron spin resonance studies of clays representative of the sedimentary evolution of the basin of Autun, Clay Miner. 13 (1978) 299–308.

[64] P.J. Michael, W.R. McWhinnie, Mössbauer and esr studies of the thermo chemistry of illite and montmorillonite, Polyhedron 8 (1989) 2709–2718.
[65] R.C. Kemp, Orthorhombic iron centres in muscovite and phlogopite micas [2], J. Phys. C Solid State Phys. 4 (1971) 10–14.
[66] B.A. Goodman, An investigation by Mössbauer and EPR spectroscopy of the possible presence of iron-rich impurity phases in some montmorillonites, Clay Miner. 13 (1978) 351–356.
[67] J. Cornejo, M.C. Hermosin, J.L. White, J.R. Barnes, S.L. Hem, Role of ferric iron in the oxidation of hydrocortisone by sepiolite and palygorskite, Clays Clay Miner. 31 (1983) 109–112.
[68] D. Olivier, J.C. Vedrine, H. Pezerat, Application de la RPE g la localisation des Substitutions isomorphiques dans les micas : Localisation du Fe3 + dans les muscovites et les phlogopites, J. Solid State Chem. 20 (1977) 267–279.
[69] K.P. Nicolini, K.C. Lombardi, W.H. Schreiner, I. Mazzaro, F. Wypych, A.S. Mangrich, Evidence of weathering stages of phyllosilicates from biotite/muscovite to kaolinite, probed by EPR spectroscopy, Mineral. Petrol. 97 (2009) 139–144.
[70] R.C. Kemp, Electron spin resonance of Fe3+ in muscovite, Phys. Stat. Sol. B 57 (1973) 79–81.
[71] Y.A. Koksharov, D.A. Pankratov, S.P. Gubin, I.D. Kosobudsky, M. Beltran, Y. Khodorkovsky, A.M. Tishin, Electron paramagnetic resonance of ferrite nanoparticles, J. Appl. Phys. 89 (2001) 2293–2298.
[72] I. Ardelean, M. Peteanu, V. Simon, F. Ciorcas, V. Ioncu, Structural investigation of Fe2O3 -TeO2 -B2O3 -SrO glasses by EPR, J. Mater. Sci. Lett. 20 (2001) 947–949.
[73] B.R. Angel, J.P.E. Jones, P.L. Hall, Electron spin resonance studies of doped synthetic kaolinite, I. Clay Miner. 10 (1974) 257–270.
[74] J. Gaite, P. Ermakoff, J. Muller, Characterization and origin of two Fe 3 + EPR spectra in kaolinite, Phys. Chem. Miner. (1993) 242–247.
[75] L.C. Bertolino, A.M. Rossi, R.B. Scorzelli, M.L. Torem, Influence of iron on kaolin whiteness: An electron paramagnetic resonance study, Appl. Clay Sci. 49 (2010) 170–175.
[76] R.E. Siqueira, M.M. Andrade, D.F. Valezi, C.E.A. Carneiro, J.P.P. Pinese, A.C.S. da Costa, D.A.M. Zaia, R. Ralisch, W.M. Pontuschka, C.L.B. Guedes, E. Di Mauro, EPR, FT-IR and XRD investigation of soils from Paraná, Brazil. Appl. Clay Sci. 53 (2011) 42–47.
[77] E. Boesmann, D. Schoemaker, Résonance paramagnétique de l'ion Fe+++ dans la kaolinite, Compt. Rend. Acad. Sci. (Paris) 252 (1961) 1931–1933.
[78] P.L. Hall, B.R. Angel, J.P.E. Jones, Dependence of spin Hamiltonian parameters E and D on labeling of magnetic axes: Application to ESR of high-spin Fe3+, J. Magn. Reson. 15 (1974) 64–68.
[79] J.P.E. Jones, B.R. Angel, P.L. Hall, Electron spin resonance studies of doped synthetic kaolinite. II, Clay Miner. 10 (1974) 257–270.
[80] T. Delineau, T. Allard, J.P. Muller, O. Barres, J. Yvon, J.M. Cases, FTIR Reflectance vs. EPR studies of structural iron in kaolinites, Clays Clay Miner. 42 (1994) 308–320.
[81] V. Luca, C.M. Cardile, Cation migration in smectite minerals: electron spin resonance of exchanged Fe3+ probes, Clays Clay Miner. 37 (1989) 325–332.
[82] A.M. Hirt, A. Banin, A.U. Gehring, Thermal generation of ferromagnetic minerals from iron-enriched smectites, Geophys. J. Int. 115 (1993) 1161–1168.
[83] C. Cracium, A. Meghea, Electron spin resonance studies of montmorillonites, Clay Miner. 20 (1985) 281–290.
[84] E. Balan, T. Allard, B. Boizot, G. Morin, J.P. Muller, Structural Fe3+ in natural kaolinites: New insights from electron paramagnetic resonance spectra fitting at X and Q-band frequencies, Clays Clay Miner. 47 (1999) 605–616.
[85] R.E. Meads, Electron spin resonance in natural kaolinites containing Fe3+ and other transition metal ions, Clay Miner. 10 (1975) 313–345.
[86] B.R. Angel, W.E.J. Vincent, Electron spin resonance studies of iron oxides associated with the surface of kaolins, Clays Clay Miner. 26 (1978) 263–272.
[87] K. Flogeac, E. Guillon, M. Aplincourt, E. Marceau, L. Stievano, P. Beaunier, Y.M. Frapart, Characterization of soil particles by X-ray diffraction (XRD), X-ray photoelectron spectroscopy (XPS), electron paramagnetic resonance (EPR) and transmission electron microscopy (TEM), Agron. Sustain. Dev. 25 (2005) 345–353.
[88] C.E.A. Carneiro, F.F. Ivashita, I.G. De Souza, C.M.D. De Souza, A. Paesano, A.C.S. Da Costa, E. Di Mauro, H. De Santana, C.T.B.V. Zaia, D.A.M. Zaia, Synthesis of goethite in solutions of artificial seawater and amino acids: A prebiotic chemistry study, Int. J. Astrobiol. 12 (2013) 149–160.
[89] D.F. Valezi, M.T. Piccinato, P.W.C. Sarvezuk, F.F. Ivashita, A. Paesano, J. Varalda, D.H. Mosca, A. Urbano, C.L.B. Guedes, E. Di Mauro, Goethite (α-FeOOH) magnetic transition by ESR, Magnetometry and Mössbauer, Mater. Chem. Phys. 173 (2015) 179–185.
[90] S. Bodeï, M. Buatier, M. Steinmann, T. Adatte, C.G. Wheat, Characterization of metalliferous sediment from a low-temperature hydrothermal environment on the Eastern Flank of the East Pacific Rise, Mar. Geol. 250 (2008) 128–141.
[91] B. Clozel, T. Allard, J.-P. Muller, Nature and stability of radiation-induced defects in natural kaolinites: new results and a reappraissal of published works, Clays Clay Miner. 42 (1994) 657–666.
[92] T. Allard, G. Calas, Radiation effects on clay mineral properties, Appl. Clay Sci. 43 (2009) 143–149.
[93] T. Allard, E. Balan, G. Calas, C. Fourdrin, E. Morichon, S. Sorieul, Radiation-induced defects in clay minerals: A review, Nucl. Instrum. Methods Phys. Res. Sect. B Beam Interact. with Mater. Atoms 277 (2012) 112–120.
[94] B. Clozel, J.M. Gaite, J.P. Muller, Al-O–Al paramagnetic defects in kaolinite, Phys. Chem. Miner. 22 (1995) 351–356.
[95] T.H. Allard, P.H. Ildefonse, L. Pérez del Villar, S.T. Sorieul, M. Pelayo, B. Boizot, E. Balan, G. Calas, Radiation-induced defects in dickites from the El Berrocal granitic system (Spain): relation with past occurrence of natural radioelements, Eur. J. Miner. 15 (2003) 629–640.
[96] J. Nicolini, B.F. Pereira, C.N. Pillon, V.G. MacHado, W.A. Lopes, J.B. De Andrade, A.S. Mangrich, Characterization of Brazilian oil shale byproducts planned for use as soil conditioners for food and agro-energy production, J. Anal. Appl. Pyrolysis 90 (2011) 112–117.
[97] P.L. Hall, B.R. Angel, J. Braven, Electron spin resonance and related studies of lignite and ball clay from South Devon, England. Chem. Geol. 13 (1974) 97–113.
[98] C. Carbone, F. Di Benedetto, P. Marescotti, C. Sangregorio, L. Sorace, N. Lima, M. Romanelli, G. Lucchetti, C. Cipriani, Natural Fe-oxide and -oxyhydroxide nanoparticles: An EPR and SQUID investigation, Mineral. Petrol. 85 (2005) 19–32.
[99] R. Alcántara, G.F. Ortiz, P. Lavela, J.L. Tirado, R. Stoyanova, E. Zhecheva, EPR, NMR, and electrochemical studies of surface-modified carbon microbeads, Chem. Mater. 18 (2006) 2293–2301.
[100] E. Zhecheva, R. Stoyanova, J.M. Jiménez-Mateos, R. Alcántara, P. Lavela, J.L. Tirado, EPR study on petroleum cokes annealed at different temperatures and used in lithium and sodium batteries, Carbon N. Y. 40 (2002) 2301–2306.
[101] T. Taub, S. Ruthstein, H. Cohen, The involvement of carbon-centered radicals in the aging process of coals under atmospheric conditions: An EPR study, Phys. Chem. Chem. Phys. 20 (2018) 27025–27035.
[102] C. Menachem, Y. Wang, J. Flowers, E. Peled, S.G. Greenbaum, Characterization of lithiated natural graphite before and after mild oxidation, J. Power Sources 76 (1998) 180–185.
[103] U. Green, K. Keinan-Adamsky, S. Attia, Z. Aizenshtat, G. Goobes, S. Ruthstein, H. Cohen, Elucidating the role of stable carbon radicals in the low temperature oxidation of coals by coupled EPR-NMR spectroscopy-a method to characterize surfaces of porous carbon materials, Phys. Chem. Chem. Phys. 16 (2014) 9364–9370.
[104] M. Ikeya, New applications of electron spin resonance. Dating, dosimetry and microscpy, Wold Scientific, Singapore, 1993.
[105] E. Morichon, T. Allard, D. Beaufort, P. Patrier, Evidence of native radiation-induced paramagnetic defects in natural illites from unconformity-type uranium deposits, Phys. Chem. Miner. 35 (2008) 339–346.
[106] C. Chen, Z. Tang, Y. Ma, W. Qiu, F. Yang, J. Mei, Physicochemical, microstructural, antioxidant and antimicrobial properties of active packaging fi lms based on poly(vinyl alcohol)/ clay nanocomposite incorporated with tea polyphenols, Prog. Org. Coatings 123 (2018) 176–184.
[107] M.A. Usolo, J.M. Lagaron, Oxygen scavenging polyolefin nanocomposite films containing an iron modified kaolinite of interest in active food packaging applications. Innov. Food Sci. Emerg. Technol. 16 (2012) 211–217.
[108] I. Ahmad, C.Y. Li, Y.G. Hsuan, R.A. Cairncross, Reaction model describing antioxidant depletion in polyethylene e clay nanocomposites under thermal aging, Polym. Degrad. Stab. 110 (2014) 318–335.
[109] D. Kibanova, A. Nieto-Camacho, J. Cervini-Silva, Lipid peroxidation induced by expandable clay minerals, Environ. Sci. Technol. 43 (2009) 7550–7555.
[110] C.C. Otto, J.L. Koehl, D. Solanky, S.E. Haydel, Metal ions, not metal-catalyzed oxidative stress, cause clay leachate antibacterial activity, PLoS ONE 9 (2014) 1–21.